

# Effect of Compositional Variation in TiO<sub>2</sub>-Based Flux-Cored Arc Welding Fluxes on the Thermo-physical Properties and Mechanical Behavior of a Weld Zone



J.B. KIM, T.H. LEE, and I. SOHN

The effect of compositional variation in TiO<sub>2</sub>-based flux-cored arc welding fluxes on viscosity, wettability, and electronegativity was studied. The thermo-physical properties of the retrieved fluxes and their relationship with the mechanical properties of the weld zone, including tensile strength and micro-Vickers hardness, after welding were identified. Microstructural observation under similar welding conditions revealed significant grain coarsening at a corrected optical basicity ( $\Lambda^{\text{corr}}$ ) of 0.62, resulting in reduced strength and hardness due to greater heat transfer. Welding fluxes containing TiO<sub>2</sub>-based simple structural units should result in greater heat transfer due to the deficiency in complex  $[\text{AlO}_4]^{5-}$  and  $[\text{SiO}_4]^{4-}$ -based structural units, as identified through spectroscopic analyses using fourier transform infrared spectroscopy, Raman spectroscopy, and X-ray photoelectron spectroscopy. The electronegativity of the retrieved fluxes was also evaluated since higher electronegativity results in greater absorption of electrons in the arc, resulting in arc condensation towards the center direction. Consequently, deeper penetration could be obtained, where the highest electronegativity was identified to be approximately 0.62 of the corrected optical basicity. Thus, both the thermal conductivity and electronegativity of the welding fluxes were identified to determine the heat transfer phenomenon during flux-cored arc welding.

<https://doi.org/10.1007/s11661-018-4624-1>

© The Minerals, Metals & Materials Society and ASM International 2018

## I. INTRODUCTION

THERE has been significant demand in consumer needs for advanced high-strength steels (AHSS) containing significant Mn and Al, including transformation-induced plasticity (TRIP) and twinning-induced plasticity (TWIP) steels, for high-rise construction, ultra-large vessels, automotive needs, and others. Research in the development of these grades of steel and applications has seen significant strides, where the high volume of deformation twinning increases the tensile strain, showing a larger strain hardening capacity than FBDP (ferrite and bainite dual-phase) and TRIP steel.<sup>[1,2]</sup> However, the greater strength and formability of these steels have been known to make these materials highly susceptible to hydrogen-delayed cracking in flux-cored arc-welded (FCAW) joints, where the hydrogen originates from the moisture in the atmosphere or

the welding fluxes. In particular, the microstructure of the heat-affected zone (HAZ), which is controlled by the heat flux during welding, seems to greatly affect the sensitivity of the cracking behavior. Furthermore, the high Mn and Al contents in the AHSS can easily oxidize, according to Kou,<sup>[3]</sup> and these oxidized inclusions in the weld zone can act as initiation points for cracking, resulting in a lower strength. Thus, to ensure optimal performance of the weld joint, it is imperative to develop welding fluxes that provide both sufficient coverage and appropriate heat fluxes to minimize welding defects.

FCAW is widely used for carbon steels, low alloy steels, stainless steels, and especially high Mn-containing steels since the flux prevents contamination from air by providing adequate surface coverage during welding. Gomes *et al.*<sup>[4]</sup> also indicated that FCAW can provide high deposition rates, minimal waste of electrodes, greater process flexibility, high weld quality, and excellent control of the weld pool. However, Spear<sup>[5]</sup> indicated that FCAW generates a substantial amount of fumes, including ozone, nitric oxide, and carbon dioxides, due to the high electrical current and flux-cored electrode.

Previous authors have indicated the importance of *shielding gases* such as Ar and CO<sub>2</sub> during arc welding,<sup>[6]</sup> and the majority of manufacturers use CO<sub>2</sub> during the

J.B. KIM, and I. SOHN are with the Department of Materials Science and Engineering, Yonsei University, 50 Yonsei-ro, Seodaemun-gu, Seoul 03722, Republic of Korea. Contact e-mail: [ilsohn@yonsei.ac.kr](mailto:ilsohn@yonsei.ac.kr) T.H. LEE is with the Mechanical Design Engineering, Hanyang University, 222 Wangsimni-ro, Seongdong-gu, Seoul 04763, Republic of Korea.

Manuscript submitted November 27, 2017.

Article published online April 17, 2018

arc welding of TRIP and TWIP steels. Although 100 pct CO<sub>2</sub> shielding gas results in significant spattering along with excessive melt downs and fusing, the use of CO<sub>2</sub> can lead to deeper bead penetration as the surface tension of the molten pool increases due to the oxygen partial pressure of CO<sub>2</sub>. Furthermore, CO<sub>2</sub> can dissociate at temperatures above 1873 K (1600 °C) and promote reaction between the molten metal and CO in the arc column and weld pool.<sup>[7]</sup> Thus, both the shielding gases and flux design are important parameters to achieve a sound weld.

According to Tseng and Chen,<sup>[8]</sup> fluxes composed of TiO<sub>2</sub> and SiO<sub>2</sub> assisted in the reduction of arc heat required in TIG (tungsten inert gas) welding to obtain deep penetration within a large cross-sectional area. This was attributed to the higher energy density in the arc with TiO<sub>2</sub>- and SiO<sub>2</sub>-containing fluxes due to the electronegativity difference, where the electronegativity of SiO<sub>2</sub> is higher than that of TiO<sub>2</sub>. Fluxes are utilized not only as a protective shield for the molten weld surface but also as an activating flux in CO<sub>2</sub> laser welding. Activating fluxes can effectively improve the absorption of the laser energy and increase the size of the molten pool. The activating flux can also affect the formation of gas pores.<sup>[9]</sup> According to Schwemmer *et al.*,<sup>[10]</sup> fluxes with low viscosity and surface tension were incapable of protecting the weld zone from the air, resulting in excessive oxidation and contamination at the metal–flux interface, while high-viscosity fluxes resulted in excess gas absorption at the interface, producing blow holes at the weld bead. However, fluxes with optimized viscosity and surface tension ensure sufficient coverage of the weld zone and confine the weld pool with deeper penetration of the arc, resulting in appropriate weld quality. Thus, welding fluxes are widely utilized in various welding processes, but there is still a general lack of detailed knowledge about designing fluxes and their impact on the mechanical behavior of the weld zone. Hence, a fundamental understanding of the thermo-physical properties of welding fluxes and their relationship to the quality of the weld zone is needed to design an optimized welding flux.

In this study, the compositional effect of TiO<sub>2</sub>-based welding fluxes, which have been identified as a potential candidate for high Mn- and Al-containing AHSS, on the thermo-physical properties, including viscosity and wettability, and their relationship to the mechanical properties of the weld zone have been investigated. Furthermore, the electronegativity and thermal conductivity of the fluxes on the weld have also been considered in determining the optimal compositional range of welding fluxes.

## II. EXPERIMENTAL PROCEDURE AND METHODS

### A. Welding Procedure

FCAW specimens were produced using the designed welding fluxes by a welding machine (P500L, Welbee, Daihen, Japan) under shielding gases of UHP Ar (99.9999 vol pct) and CO<sub>2</sub> (99 vol pct) on a SM490A

grade steel plate (KS D3515, 150 mm × 120 mm × 10 T) to simulate the welding behavior, which is used for railroad vehicles including the bogie frame and other structural applications. The steel substrate composition and physical properties of SM490A along with the composition of seven designed TiO<sub>2</sub>-based FCAW wires (1.4 Φ) are given in Table I. The wires were fed at a rate of 7 m/min using a shielding gas flow of 20 slm. The welding machine uniformly traversed through the surface of the plate with a single pass using a current of 280 A and a voltage of 30 V, as specified by the bead on the plate process, which is a single-path straight-line build-up welding on a plate.<sup>[11]</sup> The travel speed of the weld tip was constant at 0.3 m/min. Spent welding fluxes solidified above the weld bead were retrieved after a single straight-pass welding for compositional analyses, XRD (X-ray diffraction), wettability, and viscosity measurements. The retrieved fluxes were analyzed by X-ray fluorescence (XRF, S4 Explorer; Bruker AXS GmbH Karlsruhe, Germany) and the results are presented in Table II.

### B. Mechanical Testing

The weld zones of the FCAW specimens using the designed fluxes were machined to include the weld metal, the HAZ, and the base metal according to the specifications of the ASTM E8M standard. Tensile strength and micro-Vickers hardness were examined for these prepared specimens. The specific geometry is described in Figure 1.<sup>[12]</sup> Before mechanical testing, all specimens were polished up to 1 micron and etched with a 4 pct nital solution for 22 seconds. The microstructures of the etched specimens were observed using an optical microscope (BX41M, Olympus, Japan), and the detailed microstructure was observed using a field emission-scanning electron microscope (FE-SEM, JEM2000EX, JEOL, Japan) with Electron Backscatter Diffraction analysis (EBSD, AMETEK EDAX).

The hardness values of the characteristic regions, including the HAZ, weld metal (WM), and base metal (BM), were separately measured at least 5 times with a load of 490.3 mN using a micro-Micro-Vickers hardness tester (810 to 129 K, Mitutoyo, Kawasaki, Japan). The measured hardness values were averaged after excluding the highest and lowest values. The tensile strength of the fabricated specimens was obtained from a tensile testing machine (3382, Instron, MA) using a crosshead speed of 1 mm/min at room temperature. Tensile tests were performed three times to ensure reproducibility.

The average grain size was determined by the Smith and Gutterman equation, which can be expressed by Eq. [1].<sup>[13]</sup>

$$d = 3 \times (2 \times N_L)^{-1}, \quad [1]$$

where  $N_L$  is the number of intercepts per unit length of a random line on the optical images. Random straight lines were drawn on the SEM images three times. The average grain size with the standard deviations is presented in Table III.

**Table I. Composition of the Welding Fluxes for the FCAW Wires and the SM490A Steel Substrate in Weight Percent**

Designation	TiO <sub>2</sub>	Al <sub>2</sub> O <sub>3</sub>	SiO <sub>2</sub>	Na <sub>2</sub> O	K <sub>2</sub> O	Al	Mg	Si	Mn	MnO
A	50.91	11.45	5.35	0.67	0.40	3.05	3.03	6.45	18.71	0.00
B	55.45	5.78	9.47	0.61	0.36	2.77	2.75	5.85	16.98	0.00
C	50.91	1.27	15.53	0.67	0.40	3.05	3.03	6.44	18.71	0.00
D	61.09	1.27	5.35	0.67	0.40	3.05	3.03	6.45	18.71	0.00
E	59.13	1.21	9.93	0.64	0.38	2.90	2.88	6.13	17.80	0.00
F	57.44	1.20	5.03	0.63	0.37	2.87	2.85	6.06	17.59	5.98
G	54.20	1.13	4.74	0.59	0.35	2.70	2.69	5.72	16.59	11.29

Designation	C	Si	Mn	P (× 10 <sup>-2</sup> )	S (× 10 <sup>-2</sup> )
SM490A	0.17	0.19	1.51	0.84	0.24

**Table II. Composition of Retrieved Slag on the Bead with Weight Percent Using Different Shielding Gases**

Gas	Sample	TiO <sub>2</sub>	Ti <sub>2</sub> O <sub>3</sub>	MnO	Al <sub>2</sub> O <sub>3</sub>	SiO <sub>2</sub>	MgO	FeO	Corrected Optical Basicity (× 10 <sup>-2</sup> )
Ar	A	61.52	0.21	7.87	20.47	3.19	5.25	1.49	60.59
	B	64.05	0.53	9.82	12.52	6.39	4.55	2.14	61.24
	C	60.63	0.11	12.17	9.05	10.33	5.51	2.19	61.84
	D	72.82	0.43	8.55	3.20	8.20	5.20	1.85	62.35
	E	67.97	0.51	10.61	7.74	6.01	4.88	2.29	62.41
	F	68.34	0.32	11.55	8.29	4.48	5.20	1.82	63.26
	G	66.71	0.11	14.21	7.59	4.99	4.68	1.71	63.33
CO <sub>2</sub>	A	54.31	0.24	11.67	18.29	7.34	4.91	3.24	60.80
	B	56.86	0.46	12.87	11.51	10.46	4.51	3.34	61.65
	C	51.98	0.64	15.27	8.13	15.17	5.01	3.80	62.12
	D	72.73	0.73	6.68	4.02	10.95	3.21	1.67	62.39
	E	60.31	0.51	13.72	7.15	10.26	4.67	3.38	62.68
	F	60.56	0.53	16.18	7.02	8.12	4.57	3.01	63.61
	G	55.41	0.46	17.79	8.03	10.01	4.59	3.70	63.64

To correlate the compositional variations in the welding flux with the measured mechanical properties, corrected optical basicity ( $\Lambda^{\text{corr}}$ ) was employed, which can be calculated using Eq. [2].

$$\Lambda^{\text{corr}} = \frac{\sum x_i \times n_i \times \Lambda_i}{\sum x_i \times n_i}, \quad [2]$$

where  $\Lambda_i$ ,  $x_i$ , and  $n_i$  are the characteristic coefficients for each oxide constituent ' $i$ ' presented in Table IV, the mole fraction of each oxide, and the number of oxygen atoms in the molecule per mole oxide, respectively, *e.g.*, 2 for SiO<sub>2</sub>, 1 for Na<sub>2</sub>O, 1 for CaF<sub>2</sub>, and 3 for Al<sub>2</sub>O<sub>3</sub>, where two fluorine ions are assumed to be equivalent to one oxygen ion. The distribution of oxygen ions should be modified in order to consider the charge valence of the Al<sup>3+</sup> ion. Since amphoteric Al<sub>2</sub>O<sub>3</sub> can function as a network-forming acidic oxide, when networking-breaking basic oxides are sufficiently available, a correction of the mole fraction of the basic oxide that is consumed for the charge compensation for the formation of AlO<sub>4</sub>-tetrahedral structural units is implemented by deducting the concentration of the oxide starting with the basic oxide component having the largest  $\Lambda_i$ .<sup>[14]</sup>

### C. Analytical Equipment for Phase Identification and Morphological Observation

All retrieved fluxes were ground for 10 minutes to ensure that the particle sizes were under 100  $\mu\text{m}$  using a ball mill (37 × 40 × 20, Pulverisette 0, FRITSCH GmbH, Rhineland-Palatinate, Germany) for structural and wet analyses of TiO<sub>x</sub>. The titration of TiO<sub>x</sub> followed the modified Korean industrial standards procedure (KS E 3013), which has been well documented in past publications.<sup>[15]</sup> XRD analyses was conducted to qualitatively identify the fraction of crystalline and amorphous phases of each retrieved flux.

The fluxes for the thermo-physical property measurements were synthesized from reagent grade TiO<sub>2</sub>, MnO, Al<sub>2</sub>O<sub>3</sub>, SiO<sub>2</sub>, MgO, FeO, and Na<sub>2</sub>O using the composition of the spent welding flux. The rutile form of TiO<sub>2</sub> was chosen since it was thermodynamically a more stable form than anatase.<sup>[16]</sup> All reagent grade chemicals were mixed and pre-melted in a Kanthal<sup>®</sup> resistance box furnace using Pt crucibles (OD : 45 × H : 48, 45 g) for 2 hours at 1823 K (1550 °C) under a UHP Ar gas flow of 0.4 slm to obtain a homogeneous master slag.

Due to the maximum temperature limitations of the Kanthal<sup>®</sup> resistance furnace, approximately 6 wt pct

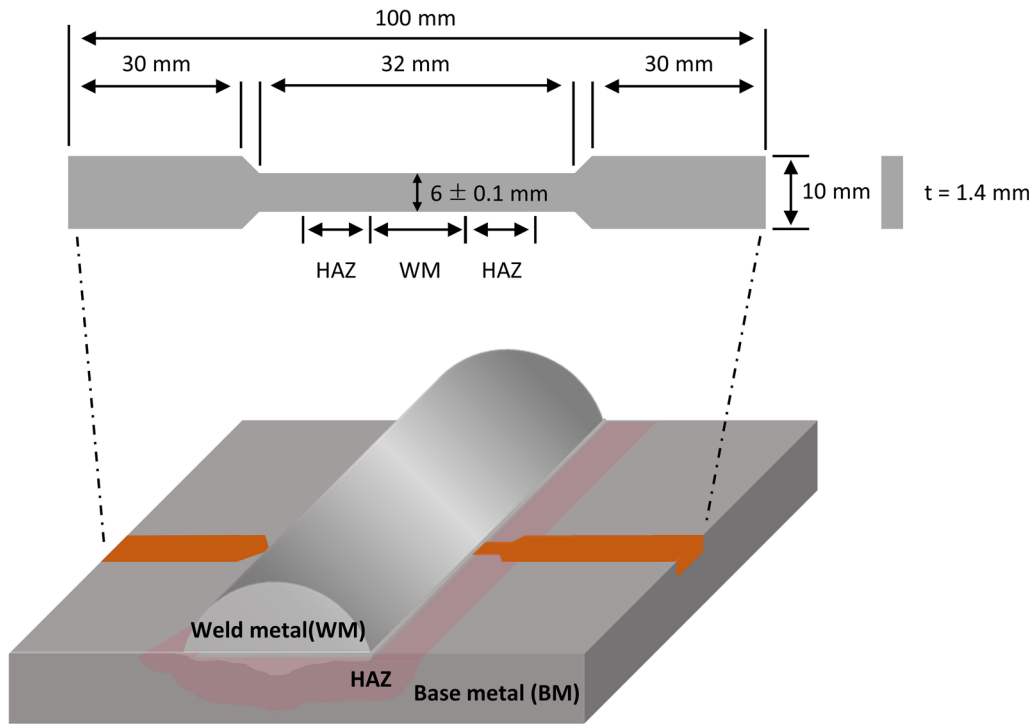


Fig. 1—Sampling location of the welded specimen for tensile testing according to the ASTM E8M standard.

**Table III. Grain Size and Area Analysis of A, D, and G Specimens**

Designation	Ar Gas			CO <sub>2</sub> Gas		
	A	D	G	A	D	G
Average grain size (SEM, $\mu\text{m}$ )	3.26 ( $\pm 0.1$ )	6.36 ( $\pm 0.92$ )	3.15 ( $\pm 0.16$ )	4.07 ( $\pm 0.7$ )	7.74 ( $\pm 1.07$ )	4.56 ( $\pm 0.19$ )
Average grain area (EBSD, $\mu\text{m}^2$ )	12.48 ( $\pm 6.01$ )	16.36 ( $\pm 10.24$ )	11.26 ( $\pm 5.97$ )	15.21 ( $\pm 8.9$ )	28.89 ( $\pm 18.52$ )	13.07 ( $\pm 10.73$ )

**Table IV. The Characteristic Coefficient ( $\Lambda_i$ ) of Each Oxide for Corrected Optical Basicity**

TiO <sub>2</sub>	MnO	Al <sub>2</sub> O <sub>3</sub>	SiO <sub>2</sub>	MgO	FeO
0.61	1.0	0.6	0.48	0.78	1.0

Na<sub>2</sub>O was added in all fluxes to decrease the melting temperature to measure the viscosity and wettability. Without Na<sub>2</sub>O, the melting points of the original spent fluxes were over 2073 K (1800 °C) on average, as calculated by FactSage<sup>®</sup> 7.0v. Although the Na<sub>2</sub>O-containing fluxes were not identical to the welding fluxes used for the FCAW, the results should provide a semi-quantitative analyses of the relationship between the thermo-physical properties and the flux composition. The viscosity and wettability were measured using a rotating viscometer and the sessile drop method, respectively, as described in detail elsewhere.<sup>[17,18]</sup>

The surface tension of the retrieved welding flux was calculated using Boni's empirical equation using the contact angle measurements of the sessile drop method on a Pt-10Rh plate in a horizontal mullite furnace at 1773 K (1500 °C) under UHP Ar gas.<sup>[19]</sup>

The viscosity measurements were conducted at 25 K interval cooling initiated from 1773 K (1500 °C) under a 0.4 slm flow of UHP Ar to prevent the molten flux from oxidizing.

#### D. Measurement of the Optical Properties

Considering the heat transfer associated with welding at high temperatures, the radiative heat transfer ability of the flux was estimated by measuring the optical properties of the fluxes. Three representative samples (A, D, G) corresponding to the low (A), transition (D), and high (G) optical basicity fluxes were chosen for optical property measurements and structural analysis. These optical properties include the apparent reflectivity ( $R_\alpha$ ) and transmissivity ( $T_\alpha$ ), which were measured using a UV-VIS-NIR spectrophotometer (ultraviolet, visible,

near-infrared, Cary 5000; Agilent) equipped with an integrating sphere between 400 to 2500 nm wavelength. The retrieved welding fluxes collected from the master slag and quenched at 1773 K (1500 °C) were polished and prepared to less than 1 mm thickness to ensure accurate measurements of the optical properties. Absorptivity ( $A_x$ ) was calculated from the simple Eq. [3].

$$R_x + A_x + T_x = 1. \quad [3]$$

### E. Structural Analyses

FTIR (Spectra100; Perkin-Elmer, Shelton CT), XPS (K-Alpha; Thermo Scientific Instrument, XPS mono, model: K-alpha by Thermo U.K.), and Raman (RD-PSH300; Photo Design, Japan) measurements of the retrieved fluxes were conducted to identify the characteristic network structure of flux and three kinds

of oxygen concentrations, namely, free oxygen ( $O^{2-}$ ), non-bridged oxygen ( $O^-$ ), and bridged oxygen ( $O^0$ ). The procedures of the spectroscopic analyses are well explained in the authors' previous work.<sup>[20]</sup>

## III. RESULTS AND DISCUSSION

### A. Mechanical Properties of Weld Specimens

The effect of the welding flux corrected optical basicity on the tensile strength of the specimen is depicted in Figure 2. The variation in tensile strength shows a 'V-shaped' trend with respect to  $\Lambda^{corr}$ , showing a minimum near 0.62 for both Ar and  $CO_2$  shielding gases. The optical images of all cracks from the tensile test specimens were observed within the HAZ. Although some deviations were observed in the measurements, the tensile strength seems to be significantly affected by changes in the flux composition. The observed tensile strength under  $CO_2$  is slightly higher than that under Ar at  $\Lambda^{corr}$  up to 0.62, but this difference becomes negligible after the minimum point beyond 0.62.

Figures 3(a) and (b) show the results of the micro-Vickers hardness test in the HAZ region and the weld metal surface as a function of  $\Lambda^{corr}$  under Ar and  $CO_2$  shielding gas atmosphere. Similar trends in the hardness values with respect to  $\Lambda^{corr}$  are observed showing again a 'V-shaped' trend with a minimum value approximately around 0.62 for both the HAZ and weld metal regions. The hardness of HAZ under  $CO_2$  is on average higher than the hardness under Ar, but the opposite behavior was identified in the weld metal. This seems to be caused by compositional differences of the fluxes during welding. Ar and  $CO_2$  gases provide different oxygen partial pressures, where welding under  $CO_2$  with higher oxygen potential increases the  $MnO$ ,  $SiO_2$ , and  $FeO$  resulting in a dilution of the  $TiO_2$  content. Thus, different compositional fluxes were synthesized with higher  $TiO_2$  and lower  $MnO$ ,  $SiO_2$ , and

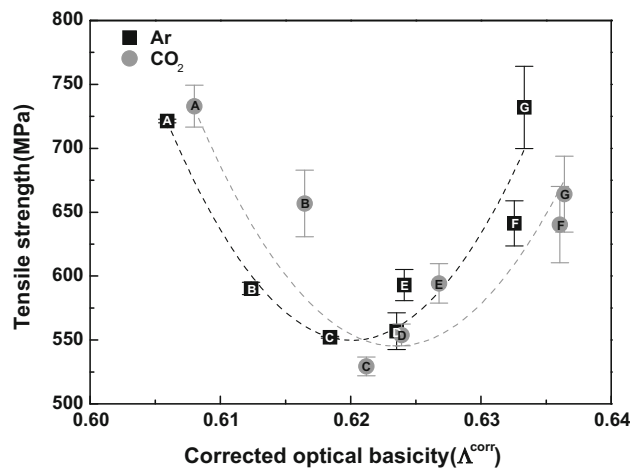


Fig. 2—Effect of corrected optical basicity on tensile strength of welded specimens.

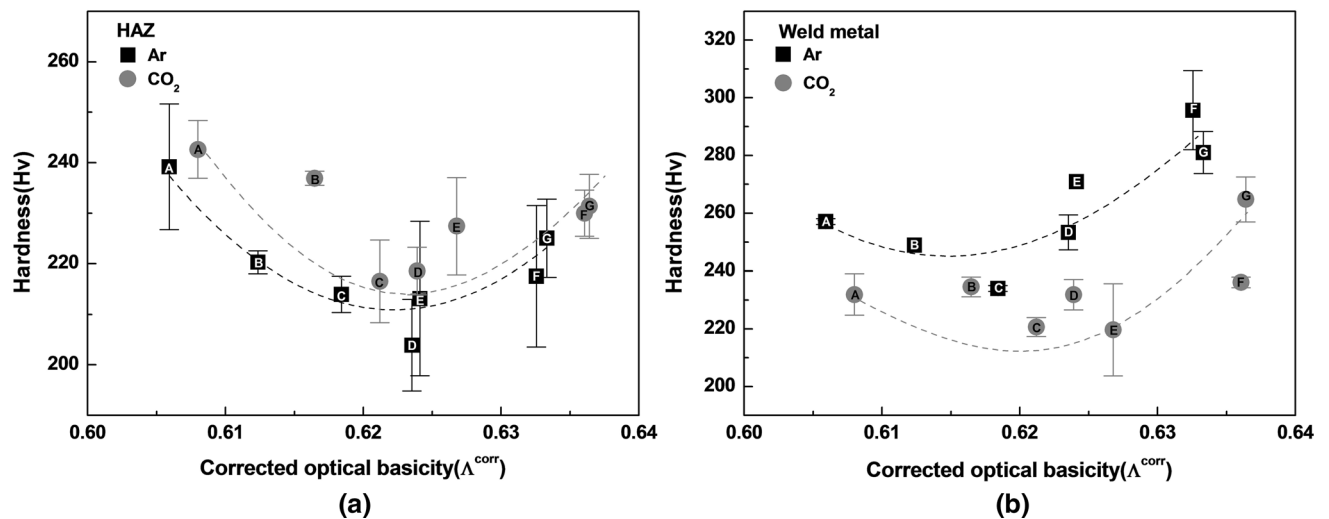


Fig. 3—Effect of the corrected optical basicity on the micro-Vickers hardness in the (a) HAZ and (b) weld metal of the welded specimens.

FeO flux for Ar compared to CO<sub>2</sub>, as described in Table II. The compositional differences, which are represented through the optical basicity, affect the arc shape and heat transfer behavior. Consequently, the grain size of the weld metal with Ar is on average smaller than the grain size with CO<sub>2</sub>. However, the hardness trend for the weld metal under CO<sub>2</sub> was not as pronounced compared to the other specimens with hardness at approximately  $\Lambda^{\text{corr}}$  of 0.61, which was quite lower than under Ar. It can be speculated that the hardness for the weld metal region can be influenced not only by the phase transformation from the applied heat, but also from the compositional changes from the filler metal, which is beyond the scope of the present work. The variation of the hardness in the HAZ region is more noticeable than the weld metal in both shielding gases,

which is mainly due to the formation of irregular-shaped phases upon fast cooling dependent on the flux composition and  $\Lambda^{\text{corr}}$ . As a general rule, a simple estimate of the tensile strength of carbon steel is approximately 3.45 times the Vickers hardness and this proportionality results in similar ‘V-shaped’ trends.<sup>[21]</sup>

### B. Morphology and Phase Analyses of the Weld Zone

Figure 4 shows the representative etched microstructure after welding with the ‘B’ flux of the three separate regions, namely, the weld metal, the HAZ, and the base metal. Similar microstructures were observed in all of the welded specimens, but with different grain sizes and amount of phases present. Comparatively, HAZ shows more noticeable grain sizes (HAZ AVG grain area :

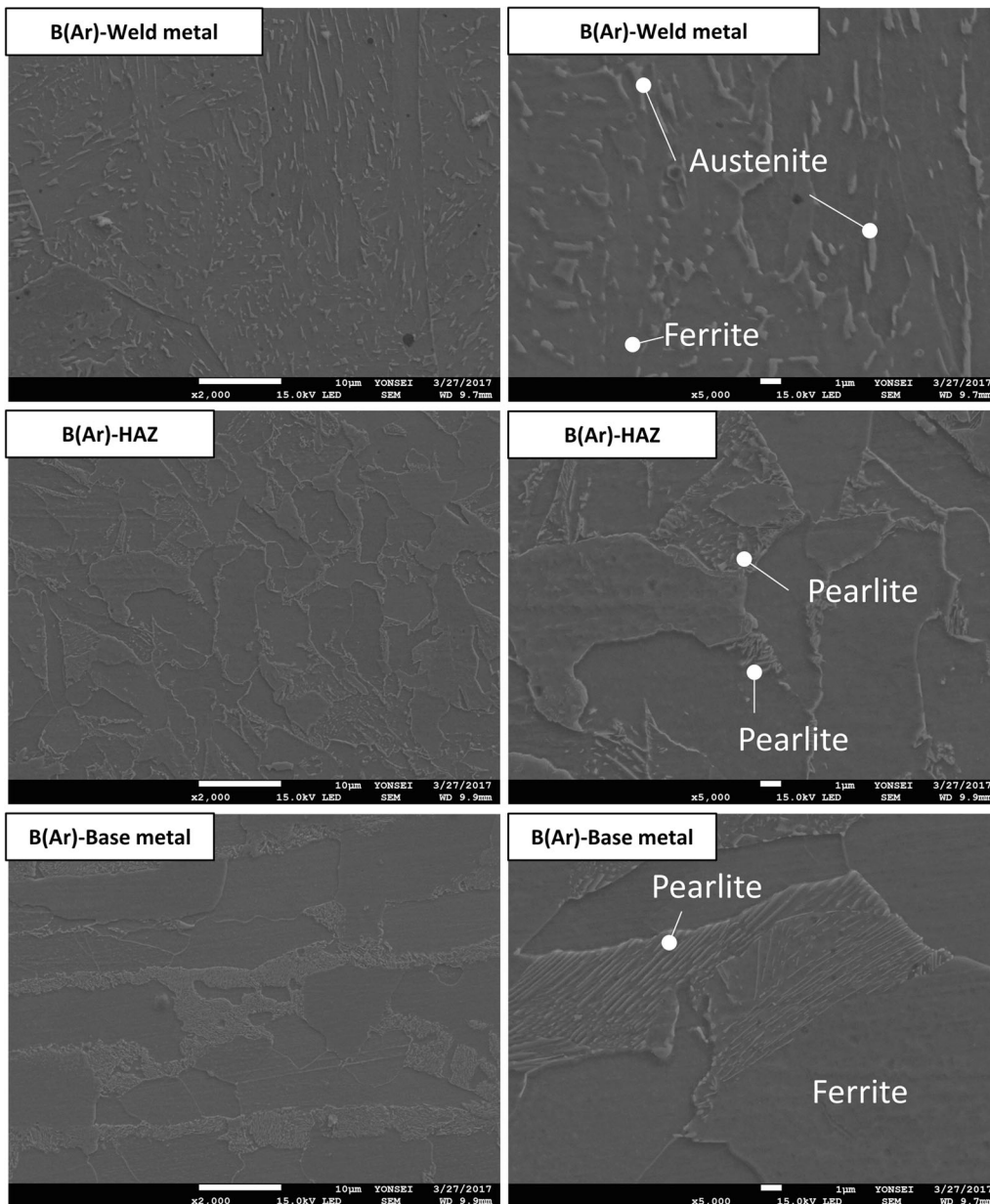


Fig. 4—SEM images of specimen B with  $\times 2000$  and  $\times 5000$  magnitude.

16.98  $\mu\text{m}^2$ ) than other characteristic regions of the weld specimen (Weld metal AVG grain area : 9.55  $\mu\text{m}^2$ ). Furthermore, the pearlite phase, which has a higher hardness (approximately 200 HV) than the ferrite phase (approximately 100 HV), is not consistently and uniformly observed in the HAZ region. The pearlite phase originates from the base metal of the rolled SM490A, where the ferrite and pearlite phases are stacked layer by layer. Needle-like ferrite can be identified in the weld metal region, and a higher hardness can be expected. Although pearlite is intermittently present within the

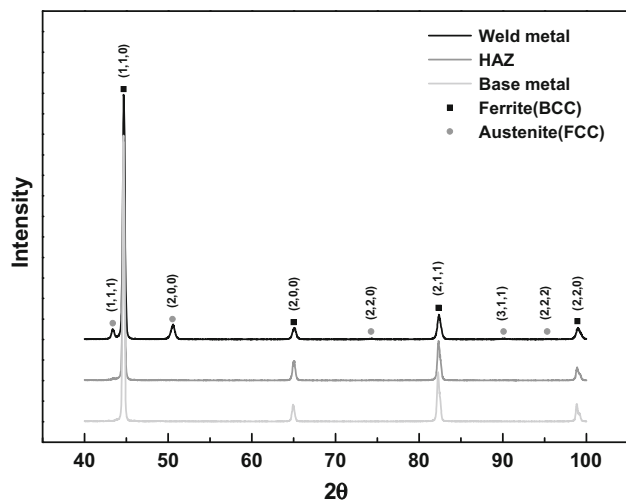


Fig. 5—X-ray diffraction pattern of each phases of welded metal of specimen D with Ar welding atmosphere conditions.

HAZ region, the presence of small grain size of austenite and needle-like ferrite in the weld metal region results in HAZ with a slightly lower hardness than the weld metal.

X-ray diffraction was conducted on the surface of the representative D specimen under an Ar shielding gas for each individual characteristics of the weld zone. Figure 5 shows the characteristic peaks corresponding to the center of these regions within the specimen. The austenite phase in the weld zone is prominent under rapid cooling conditions to room temperature directly after welding, details of which have been provided in past publications.<sup>[22,23]</sup>

In general, the specimens used in the present work showed a low fraction of austenite phase only in the weld metal, with the dominant ferrite phase identified for all regions by the SEM images and XRD results, irregular ferrite is pronounced in the HAZ near the weld metal due to rapid quenching under air to room temperature. It has also been verified that different grain sizes and the particular morphology of the irregular ferrite result in different tensile strengths, where a larger grain size results in lower strength.<sup>[24,25]</sup>

In general, the grain size of polycrystalline materials is inversely correlated to the mechanical properties, where larger average grain sizes result in lower mechanical properties.<sup>[26,27]</sup> The average grain size can be obtained from the Hall–Petch relationship, and a recently modified equation has been deduced.<sup>[26]</sup> The grain size analysis from Figure 6 is provided in Table III, and the tensile strength measurements seem to be consistent with the Hall–Petch relationship. The specimen of D has a larger average grain size than A and G in both Ar and CO<sub>2</sub> conditions, but the effect of CO<sub>2</sub> is more pronounced than that of Ar, as the average grain size with

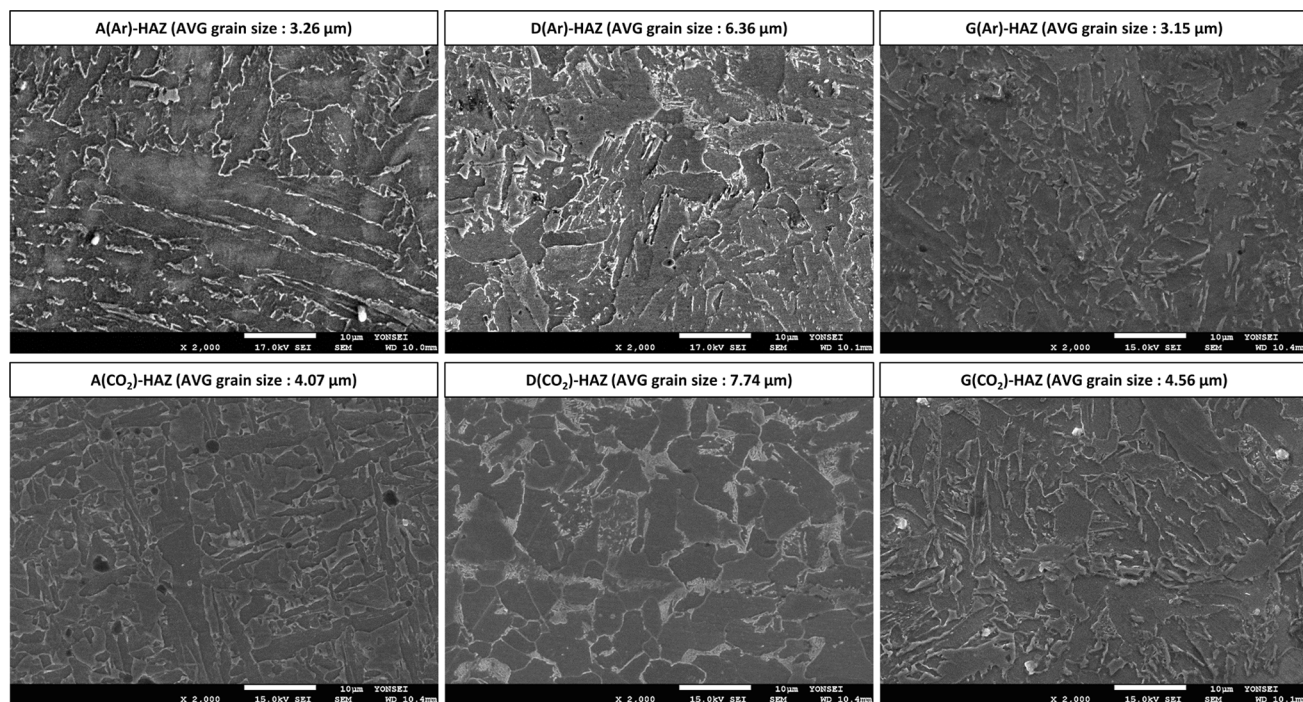


Fig. 6—SEM images of specimen A, D, and G with  $\times 2000$  magnitude prepared with Ar and CO<sub>2</sub> welding atmosphere conditions.

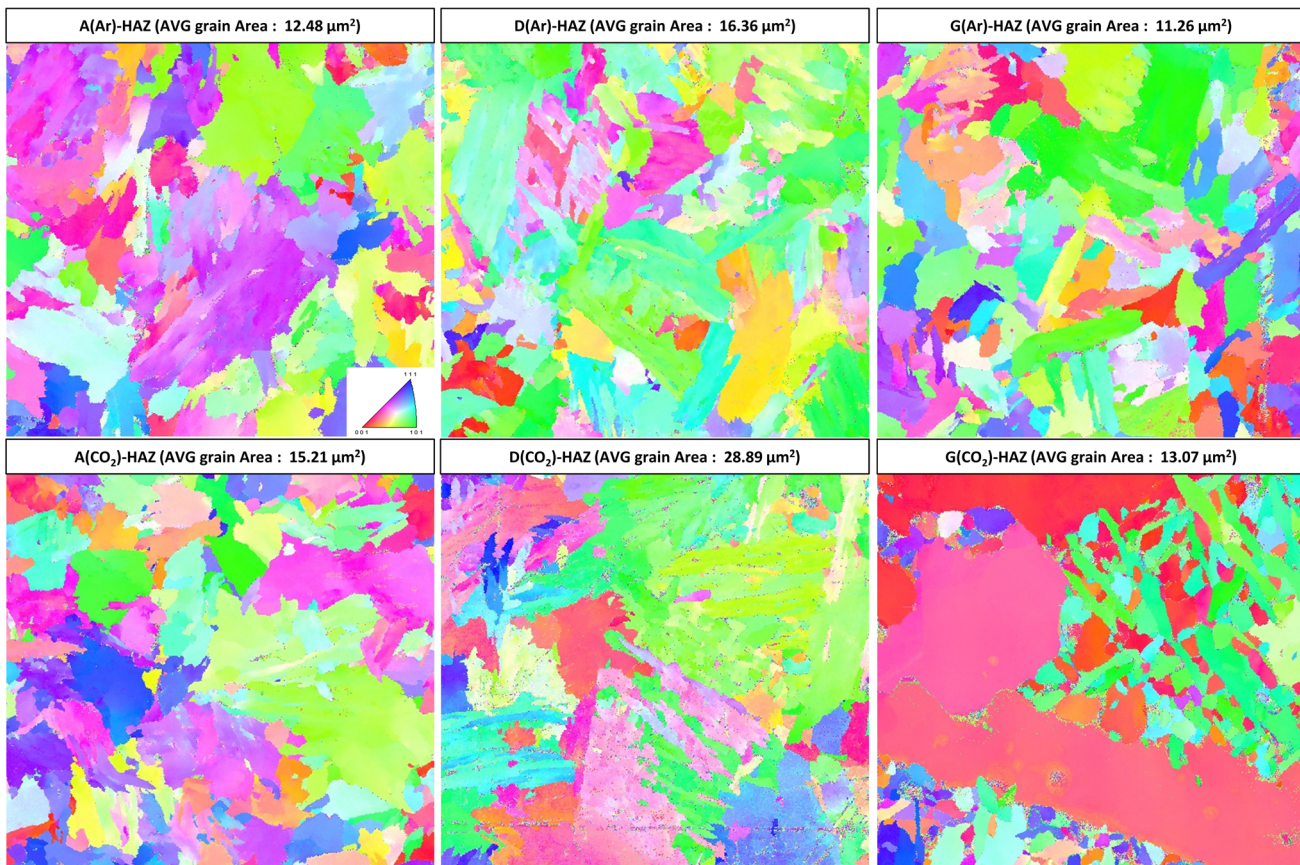


Fig. 7—EBSD inverse pole figures of specimen A, D, and G with 0.1  $\mu\text{m}$  step size and  $100 \times 100 \mu\text{m}$  area prepared with Ar and CO<sub>2</sub> welding atmosphere conditions.

CO<sub>2</sub> is slightly higher than that of Ar. The needle-like irregular ferrite phase is more prevalent in the A and G specimens. Thus, the tensile strength of these specimens should be higher than those of other specimens using different flux-cored wires since all cracks occurred in HAZ during the strength test. It is the reason why grain size analysis on HAZ only was examined.

EBSD results presented in Figure 7 and Table III show the average grain area trend to correspond well with the SEM grain size analysis of the HAZ under both CO<sub>2</sub> and Ar atmosphere. The trend of the tensile strength with the grain size and area analysis is comparable.

### C. Heat Transfer Behavior During Flux-Cored Arc Welding

It is well known that the grain growth in polycrystalline materials is closely associated with the exposed heat. During welding, the thermal energy should be transferred through the flux layer to the weld metal area, but the heat flux can be significantly modified with the flux composition and its subsequent thermal properties similar to continuous casting mold fluxes.<sup>[28]</sup> Past works revealed that the effect of compositional changes in fluxes on the heat transfer and viscosity can be significant due to the compositional effect on the structural

units of the flux and subsequently the thermal conductivity through phonon vibrations.<sup>[28–31]</sup> According to Lee and Kingery,<sup>[32]</sup> the total thermal conductivity of oxide can be presented by the summation of the conduction and radiation. The conductive heat transfer through phonon vibrations is proportional to the reciprocal of temperature above the Debye characteristic temperature. In welding fluxes, the heat transfer can be increased by polymerizing the structural units of the melts with the addition of acidic oxides such as SiO<sub>2</sub> and Al<sub>2</sub>O<sub>3</sub> in the fully liquid state.<sup>[29,33,34]</sup>

In general, the radiative heat transfer has been estimated to be approximately 10 to 20 pct of the conductive heat transfer in alkali silicate melts.<sup>[35–37]</sup> However, partially crystallized fluxes tend to inhibit radiative heat transfer even at low crystallinity. Furthermore, the radiative heat transfer becomes relatively small above 15 pct crystallinity in volume.<sup>[36]</sup> Figure 8(a) through (c) shows the absorptivity, transmittance, and reflectivity values measured using UV-VIS-NIR spectrophotometry, respectively. Retrieved spent flux samples were machined to less than 1 mm thickness, and the representative measurements for flux ‘D’ are presented. The results indicate that most of the incident light is absorbed by the flux film, whereas transmittance and reflectivity are lower than 1 pct within the ultraviolet to visible range of the incident



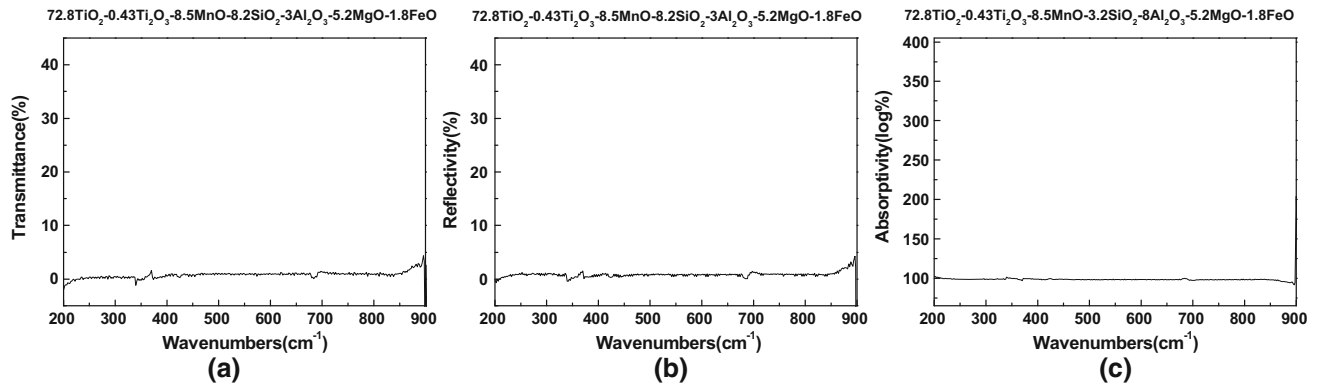


Fig. 8—UV-VIS-NIR spectrophotometer results of (a) measured transmittance, (b) reflectivity, and (c) calculated absorptivity of 72.8TiO<sub>2</sub>-0.42Ti<sub>2</sub>O<sub>3</sub>-8.5MnO-8.2SiO<sub>2</sub>-3Al<sub>2</sub>O<sub>3</sub>-5.2MgO-1.8FeO retrieved welding flux with Ar welding atmosphere condition.

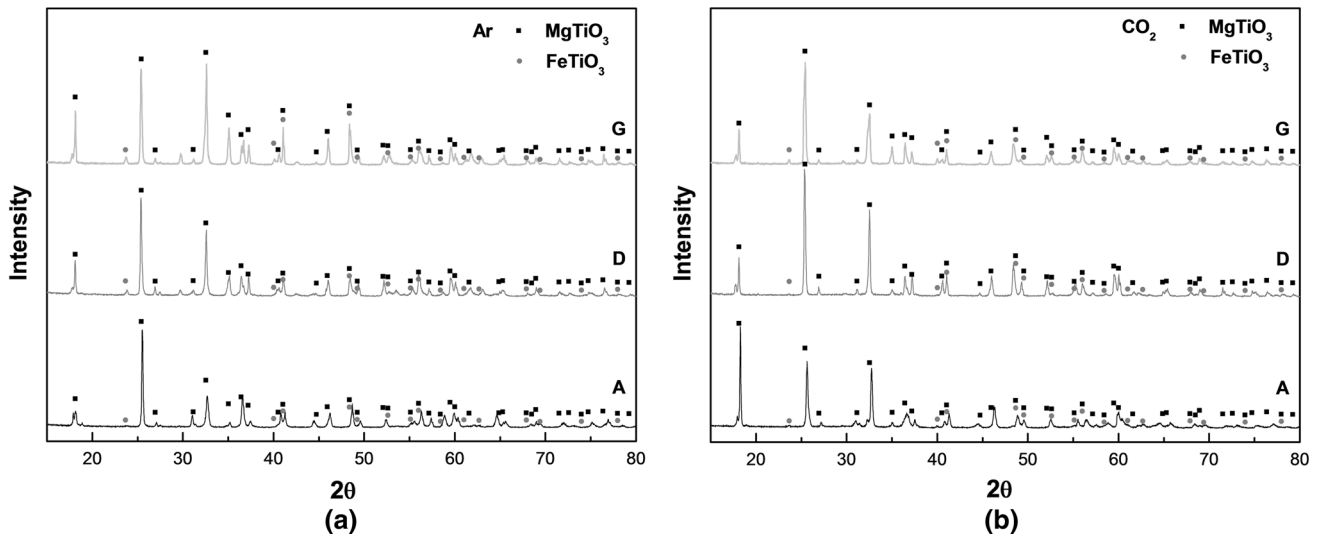


Fig. 9—X-ray diffraction pattern for crystallinity analyses of each A, D, and G retrieved welding flux formed in (a) Ar and (b) CO<sub>2</sub> welding atmosphere conditions.

radiation. Thus, it could be assumed that the radiative heat transfer to the weld pool through the TiO<sub>2</sub>-rich welding fluxes is negligible and that the bulk of the heat transfer is dominated by conduction and subsequent phonon vibration modes. In addition, radiation heat transfer is not considerable in FCAW since fluxes were suddenly solidified by the air after the welding process.

Figures 9(a) and (b) show the characteristic XRD patterns of the retrieved fluxes of A, D, and G under Ar and CO<sub>2</sub>, respectively. All solidified fluxes after welding are 100 pct crystalline with MgTiO<sub>3</sub> and FeTiO<sub>3</sub>, which have a melilite structure. This high tendency of crystallization of the fluxes deduced from the XRD analyses suggests that the total heat is likely transferred through conduction without radiative heat transfer. The high crystallinity observed for the present fluxes can be associated with the high TiO<sub>2</sub> content, resulting in higher melting temperatures and lower viscosity, which enhance diffusivity in the melt and accelerate nucleation and growth of crystals.

#### D. Viscosity and Surface Energy of Welding Fluxes

The heat transfer through the flux can also be affected by the thermodynamic properties of viscosity and surface energy, which correlate to a surface coverage phenomenon. Figure 10 shows a digital image of the sessile drop contact angle measurements of the fluxes on a Pt-10Rh plate at 1773 K (1500 °C) under an Ar and CO<sub>2</sub> atmosphere. The enlarged image of the interface between the substrate and all fluxes shows almost complete wetting with a contact angle measurement near 0 degrees.

According to Kim and Sohn<sup>[20]</sup> and Jung and Min,<sup>[38]</sup> the surface tension should decrease with higher  $\Lambda^{corr}$ . Their researches indicated basic oxides such as MgO and MnO have to be dissociated at high temperature and supplies O<sup>2-</sup>, which breaks complex network structure. Especially, TiO<sub>2</sub> develops simple network structure comparable to SiO<sub>2</sub> and Al<sub>2</sub>O<sub>3</sub>. Thus, addition of TiO<sub>2</sub> in flux system results in increased concentration of O<sup>-</sup>. Consequently, simple TiO<sub>2</sub>-based structures were much

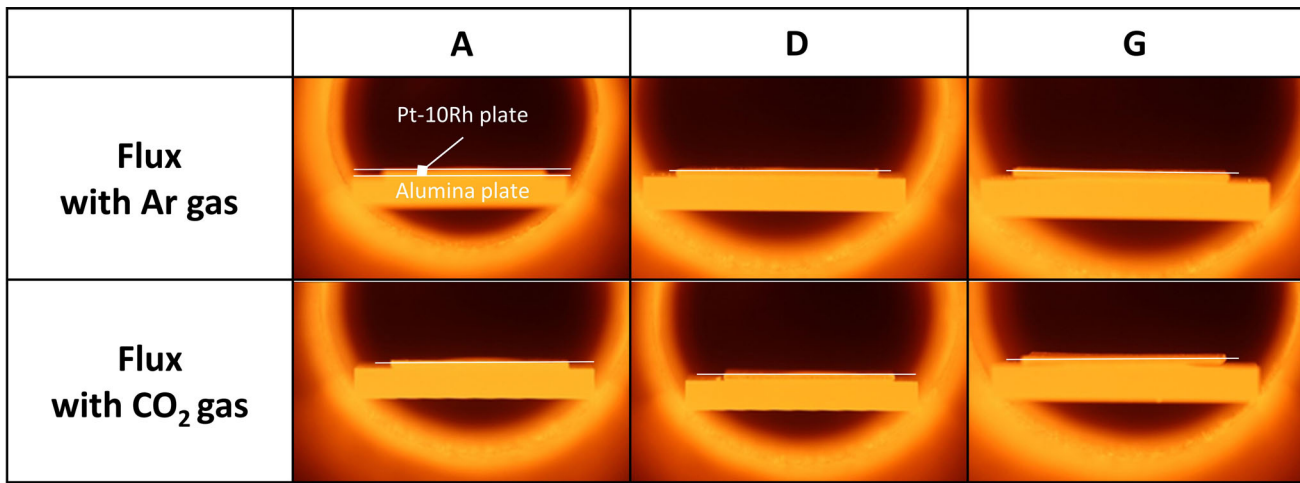


Fig. 10—Measured surface tension on Pt-10Rh plate with A, D, and G synthesized welding fluxes in horizontal mullite furnace at 1773 K.

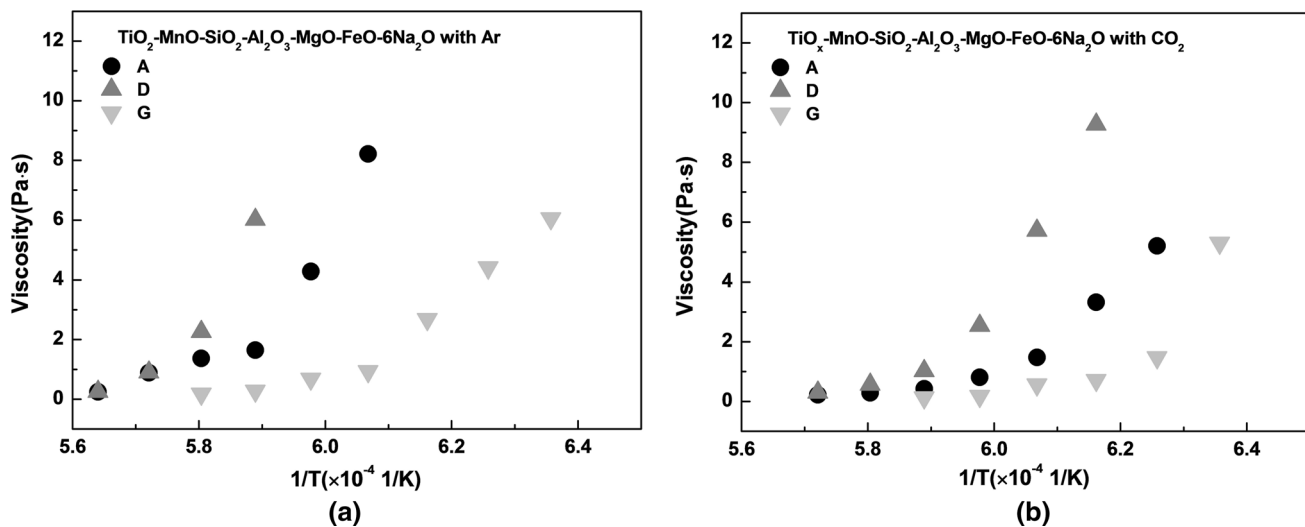


Fig. 11—Measured viscosity of TiO<sub>x</sub>-MnO-SiO<sub>2</sub>-Al<sub>2</sub>O<sub>3</sub>-MgO-FeO synthesized welding flux with 6 wt pct Na<sub>2</sub>O addition as a fusing agent with reciprocal temperature ( $\times 10^{-4}$  1/T) considering (a) Ar and (b) CO<sub>2</sub> welding conditions.

easily connected with a Pt-substrate by van der Waals forces using O<sup>-</sup> and O<sup>2-</sup> ions. As a result of high concentration of basic oxide and TiO<sub>2</sub> in the welding flux, the wetting could be fully realized.

Significant variations in the surface energies can be observed contrary to the contact angle measurements, which were near full wetting at less than 1° at 1773 K (1500 °C). It should also be noted that full coverage of the welding flux above the bead after the welding process was observed in all specimens. Thus, it would seem that complete wetting by the flux is observed during welding for the present flux compositions. The high TiO<sub>2</sub>-containing flux shows much lower contact angles than those in Kim and Sohn's<sup>[20]</sup> results due to the higher amount of TiO<sub>2</sub>. The particular TiO<sub>1</sub> structural units formed during the welding process affect the interfacial tension, which will be discussed in detail later.

From the wettability of the fluxes, it can be speculated that the bead coverage by the TiO<sub>2</sub>-based welding fluxes

for the compositional range of the present work is comparable and is not a factor for distinguishing the heat transfer variation and subsequent microstructure. Thus, it was initially speculated that the flux viscosity may indirectly have a more dominant role than the surface energy factor in controlling the heat transfer, where the viscosity can be correlated to the characteristic structural units of the flux melt.

The viscosity for the various fluxes as a function of reciprocal temperature under Ar and CO<sub>2</sub> atmospheres is shown in Figures 11(a) and (b), respectively. The measured viscosity of D is slightly higher than the viscosities of A and G at the fully molten flux in both Ar and CO<sub>2</sub> fluxes, but significant differences between the fluxes at temperatures above 1773 Ks could not be distinguished. However, the degree of polymerization for welding flux D was higher in comparison to other fluxes in terms of the viscosity. However, although the viscosity can affect the spreading phenomenon

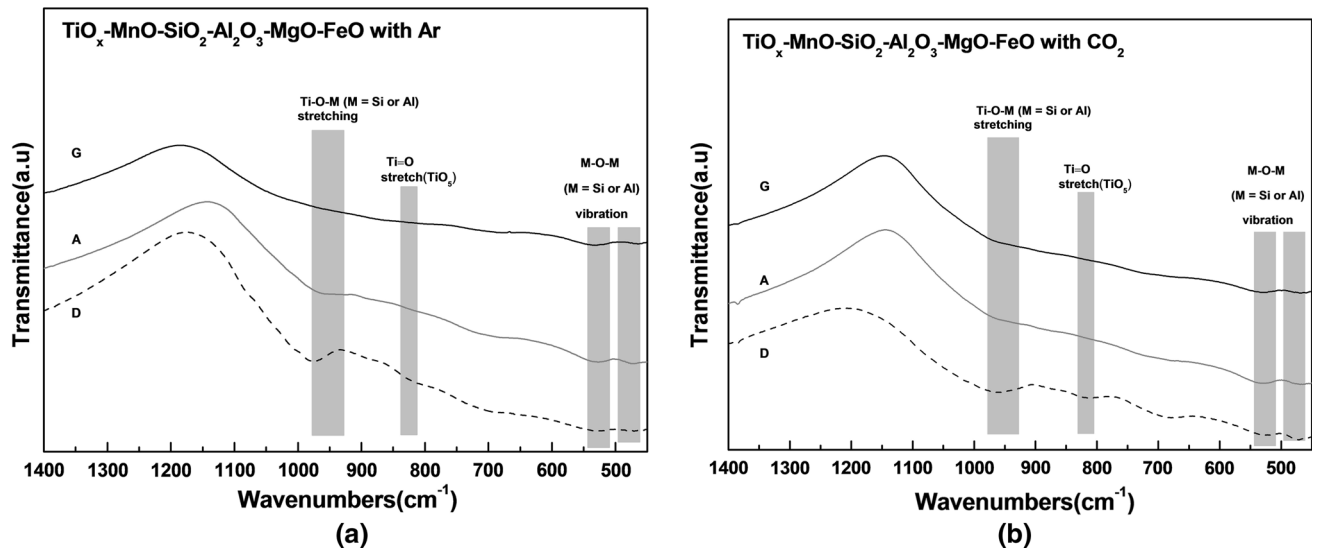


Fig. 12—FTIR spectra of  $\text{TiO}_x\text{-MnO-SiO}_2\text{-Al}_2\text{O}_3\text{-MgO-FeO}$  retrieved welding fluxes on the bead with (a) Ar and (b)  $\text{CO}_2$  welding atmosphere conditions.

according to Tanner's law, the overall extremely low viscosities of A, D, and G  $\text{TiO}_2$ -containing welding fluxes resulted in negligible affects, and full coverage was observed across the compositional range of this work.<sup>[39]</sup>

#### E. Structural Analyses and Its Effect on Heat Transfer

The structural units of the flux melts were qualitatively identified using FTIR analyses, which is depicted in Figures 12(a) and (b). The characteristic vibrations at approximately  $450$  and  $550\text{ cm}^{-1}$  correspond to the M-O-M (M = Si or Al) vibrations. The vibration at approximately  $850\text{ cm}^{-1}$  can be assigned to the Ti-O-Ti stretching vibration in high  $\text{TiO}_2$ -containing fluxes according to Sohn and Min.<sup>[40]</sup> Furthermore, Reynard and Webb<sup>[41]</sup> also indicated that peaks in the range of  $840$  to  $900\text{ cm}^{-1}$  are caused by the presence of one short Ti=O stretching vibration in the  $[\text{TiO}_5]^{6-}$  polyhedron. According to Park and Sohn,<sup>[42]</sup> the characteristic vibration at  $950\text{ cm}^{-1}$  coincides with the Ti-O-Si structural units. However, in the present flux system, the  $[\text{AlO}_4]^{5-}$  tetrahedral structure can also interact with the  $[\text{SiO}_4]^{4-}$  and  $[\text{TiO}_4]^{4-}$  tetrahedral structural units when sufficient  $\text{Al}_2\text{O}_3$  is present, possibly forming Ti-O-Al and Ti-O-Si structural units.

It is observed that complex network structures are not present in the compositional range of the present work and are likely dissociated by the basic oxides including MnO and FeO. According to the FTIR results, complex network structures from silicates, aluminates, or aluminosilicates are not detected, and the comparatively simpler network structures of Ti-O-M and Ti=O are prevalent in these  $\text{TiO}_2$ -rich welding flux compositions in the order of D, A, and G.

To reinforce the FTIR results, Raman analyses of the as-quenched fluxes were conducted, and the results are depicted in Figure 13, with the reference characteristic

structural units presented in Table V. The characteristic peaks at approximately  $490$  and  $530\text{ cm}^{-1}$  correspond to the 4-membered  $(\text{Si, Al})_4$  and 3-membered  $(\text{Si, Al})_3$  ring structures, respectively. The characteristic peaks are shifted to lower frequencies from the reference of the  $[\text{SiO}_4]^{4-}$  ring structure in the presence of  $[\text{AlO}_4]^{5-}$ , since the bonding strength of Al-O is comparably weaker than that of Si-O.<sup>[43]</sup> According to Hess *et al.*,<sup>[44]</sup> edge-sharing and corner-sharing  $[\text{TiO}_6]^{9-}$  structural units are pronounced at  $650$  and  $750\text{ cm}^{-1}$ , respectively. Those structures comprise the network structure, which interact with the  $[\text{AlO}_4]^{5-}$  and  $[\text{SiO}_4]^{4-}$  tetrahedral structures. In addition, the characteristic peaks of the  $[\text{TiO}_5]^{6-}$  polyhedral structural units can be found at  $645$  and  $717\text{ cm}^{-1}$ , since Ti-O bonds in  $[\text{TiO}_5]^{6-}$  have similar bonding distances to  $[\text{TiO}_6]^{9-}$ , but with one Ti=O bond, resulting in slightly lower frequencies compared to  $[\text{TiO}_6]^{9-}$ . Furthermore, other researchers have also revealed that characteristic peaks near  $750\text{ cm}^{-1}$  correspond to the  $[\text{TiO}_4]^{4-}$  tetrahedral structural units. Although various  $[\text{TiO}_i]$ -structural units overlap within a narrow range of frequencies, only  $[\text{TiO}_4]^{4-}$  and  $[\text{TiO}_5]^{6-}$  structures can be formed in the present high  $\text{TiO}_2$ -containing welding fluxes according to the titration analyses of  $\text{TiO}_2$  presented in Tables II and V. Thus, the peaks at approximately  $645\text{ cm}^{-1}$  can be assigned to the  $[\text{TiO}_5]^{6-}$  polyhedral structural units, which can exist as edge-sharing oligomers of self-connecting  $(\text{TiO}_5\text{-TiO}_5)$  structures and corner-sharing oligomers connected with  $[\text{AlO}_4]^{4-}$  or  $[\text{SiO}_4]^{4-}$  tetrahedral structures of  $(\text{TiO}_5\text{-AlO}_4$  or  $\text{SiO}_4)$ . Similarly, the peak at approximately  $750\text{ cm}^{-1}$  can be attributed to the  $[\text{TiO}_4]^{4-}$  tetrahedral structural units. According to McMillan and Piriou,<sup>[45]</sup> the combined stretching vibration of Al and Si-O should be detected at the wavenumbers of  $890$ ,  $900$ ,  $980$ , and  $1050\text{ cm}^{-1}$ , where these peaks directly indicate the degree of polymerization of the

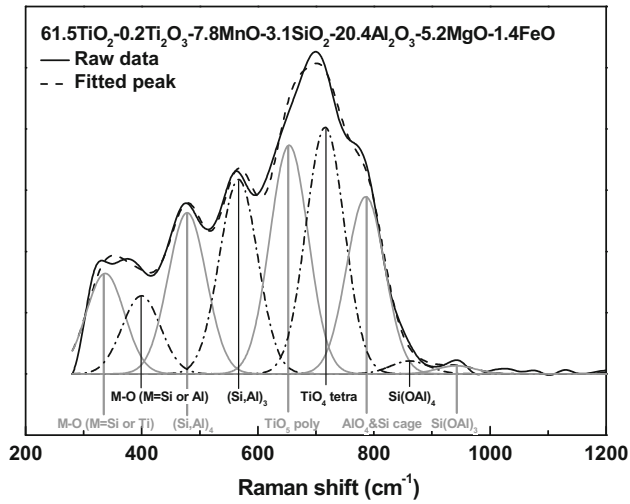


Fig. 13—A typical Raman spectra of 61.5TiO<sub>2</sub>-0.21Ti<sub>2</sub>O<sub>3</sub>-7.8MnO-3.1SiO<sub>2</sub>-20.4Al<sub>2</sub>O<sub>3</sub>-5.2MgO-1.4FeO retrieved welding flux with deconvoluted peaks.

structural units. Detailed information about the peaks can be readily obtained from a previous study.<sup>[17]</sup>

The characteristic peak variation with  $\Lambda^{\text{corr}}$  under Ar and CO<sub>2</sub> atmospheres is presented in Figures 14(a) and (b), respectively. It can be speculated from the Raman results that most of the complex network structures formed from the [AlO<sub>4</sub>]<sup>5-</sup> and [SiO<sub>4</sub>]<sup>4-</sup>-tetrahedral structural units are depolymerized within the compositional range of the present work, since the percent of characteristic vibrations such as M-O (M = Si or Al), 3- or 4-membered rings (Si, Al)<sub>t</sub>, and [AlO<sub>4</sub>]<sup>5-</sup> and Si cage motion is at most 15 pct. Moreover, the vibration peaks beyond 1000 cm<sup>-1</sup>, which correspond to the [AlO<sub>4</sub>]<sup>5-</sup> and [SiO<sub>4</sub>]<sup>4-</sup>-tetrahedral structures, are not present in the present high TiO<sub>2</sub>-containing welding fluxes, whereas [TiO<sub>5</sub>]<sup>6-</sup>-polyhedral and [TiO<sub>4</sub>]<sup>4-</sup>-tetrahedral structural units are dominant. Thus, the majority of the structural units present in the TiO<sub>2</sub>-rich welding fluxes are composed of comparatively simpler TiO<sub>t</sub>-based structural units and much lower viscosities, and negligible changes in the contact angle were observed in the fully liquid phase at high temperatures. These dominant

Table V. Deconvoluted Characteristic Raman Peaks

Ratio	Structural Units (cm <sup>-1</sup> )								
	M-O (Si, Al)	M-O (Si, Al)	4-Membered Ring	3-Membered Ring	Edge-Sharing TiO <sub>5</sub>	TiO <sub>4</sub> Tetra	AlO <sub>4</sub> , Si Cage Motion	Si(OAl) <sub>4</sub>	Si(OAl) <sub>3</sub>
Ref	335	430	490 (~540)	530 (~590)	645	750	767 (~800)	850	900
A (Ar)	334	399	477	564	652	714	786	861	934
D (Ar)	332	401	465	563	648	720	780	855	928
G (Ar)	334	403	472	563	649	719	779	858	926
A (CO <sub>2</sub> )	334	400	471	560	650	721	785	859	934
D (CO <sub>2</sub> )	333	401	476	562	649	718	781	854	935
G (CO <sub>2</sub> )	333	403	769	562	653	720	783	852	930

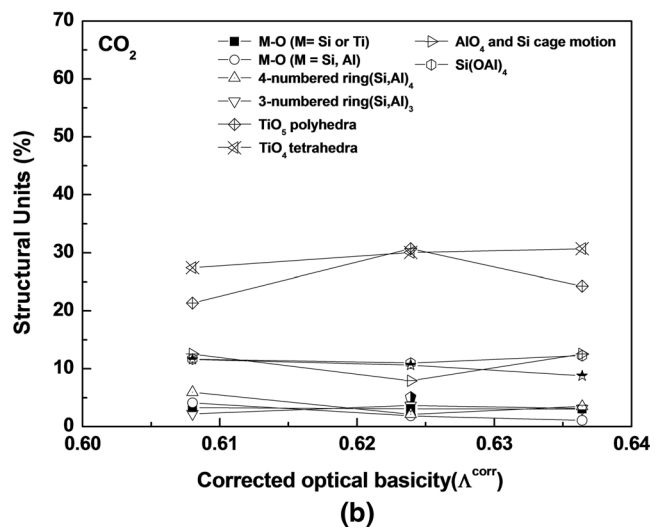
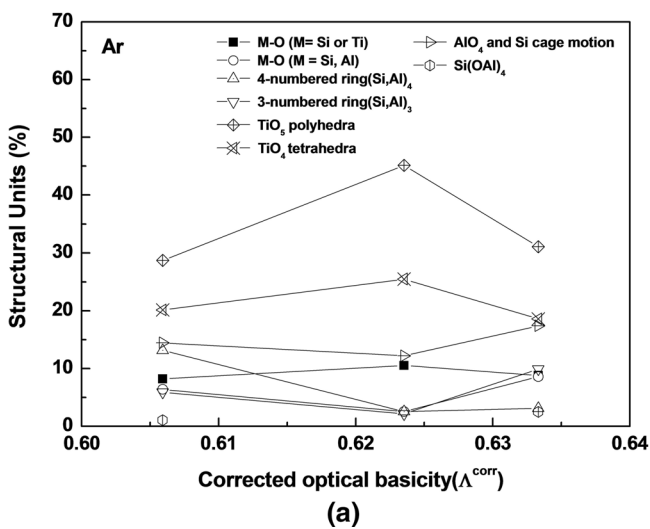


Fig. 14—The fraction of structural units of Raman spectra of TiO<sub>x</sub>-MnO-SiO<sub>2</sub>-Al<sub>2</sub>O<sub>3</sub>-MgO-FeO retrieved welding fluxes formed in (a) Ar and (b) CO<sub>2</sub> welding atmosphere conditions.

TiO<sub>1</sub>-based structural units determine the overall degree of polymerization, and subsequently, the heat transfer by conduction could be anticipated from the aforementioned spectroscopic analyses. Since the available [TiO<sub>1</sub>]-structural units and the amount are the highest

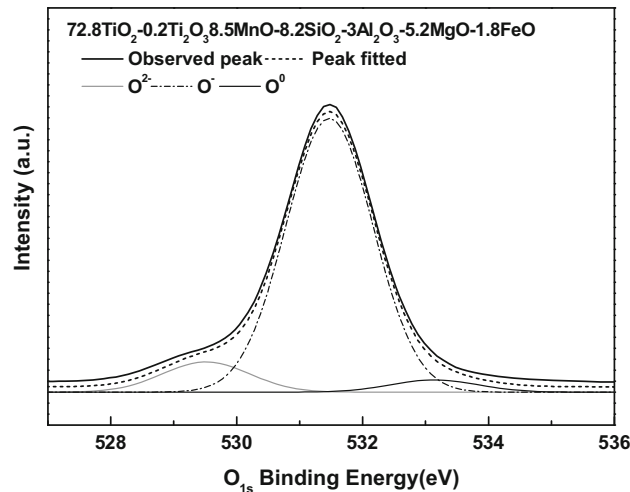
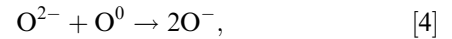


Fig. 15—Deconvoluted XPS spectra as a function of O<sub>1s</sub> binding energy for 72.8TiO<sub>2</sub>-0.42Ti<sub>2</sub>O<sub>3</sub>-8.5MnO-8.2SiO<sub>2</sub>-3Al<sub>2</sub>O<sub>3</sub>-5.2MgO-1.8FeO retrieved welding flux.

for flux D, specimen D shows a larger average grain size than A and G for both Ar and CO<sub>2</sub>.

The XPS results also show similar trends to the FTIR and Raman analyses, which are supported by analyses of the three different types of oxygen anions. According to Toop and Samis,<sup>[46]</sup> the depolymerization process of network structures can be expressed according to reaction.<sup>[4]</sup>



where O<sup>2-</sup> breaks the O<sup>0</sup> (bridged oxygen) of the complex network structure, generating two O<sup>-</sup> ions (non-bridged oxygens), *i.e.*, a typical example of deconvoluted oxygen species, and the O<sub>1s</sub> binding energies are described in Figure 15 and Table VI. With the change in  $\Lambda^{corr}$ , the fraction of the individual oxygen anion species from the XPS spectra is deconvoluted using the Gaussian method, as depicted in Figures 16(a) and (b). The fractions of O<sup>2-</sup> and O<sup>0</sup> are minimized with the D welding flux, whereas O<sup>-</sup> is maximized in both Ar and CO<sub>2</sub> atmosphere. It can be deduced that the complex network structures formed by the [AlO<sub>4</sub>]<sup>5-</sup> and [SiO<sub>4</sub>]<sup>4-</sup>-tetrahedral structural units are depolymerized and O<sup>2-</sup> is consumed by the [TiO<sub>4</sub>]<sup>4-</sup> tetrahedral structural units to form [TiO<sub>5</sub>]<sup>6-</sup> or [TiO<sub>6</sub>]<sup>9-</sup> structural units, consequently increasing the fraction of O<sup>-</sup>. As the structural units of the silicates, aluminates, or

Table VI. O<sub>1s</sub> Binding Energy of the XPS Spectra

No.	O <sup>2-</sup> (eV)	FWHM (eV)	O <sup>-</sup> (eV)	FWHM (eV)	O <sup>0</sup> (eV)	FWHM (eV)
A (Ar)	529.76	1.62	531.35	1.61	533.09	1.53
D (Ar)	529.52	1.62	531.47	1.61	533.16	1.61
G (Ar)	529.46	1.62	531.44	1.52	533.10	1.35
A (CO <sub>2</sub> )	529.78	1.52	531.52	1.62	532.94	1.59
D (CO <sub>2</sub> )	529.46	1.47	531.74	1.57	533.10	1.58
G (CO <sub>2</sub> )	529.16	1.59	531.69	1.55	532.98	1.58

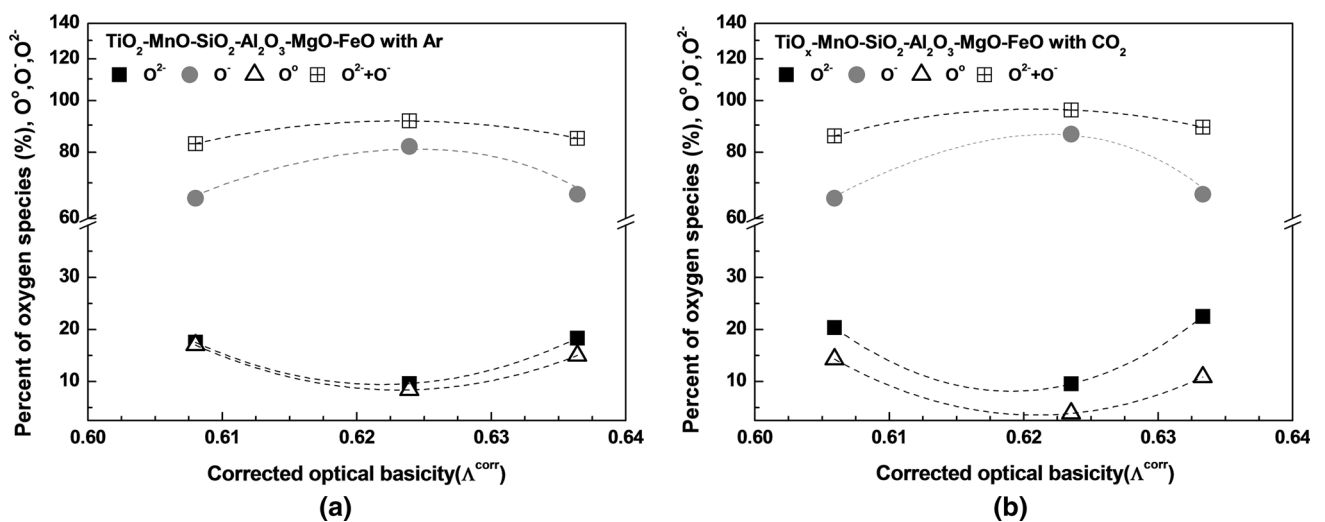


Fig. 16—Effect of corrected optical basicity on the percentage of oxygen species of TiO<sub>x</sub>-MnO-SiO<sub>2</sub>-Al<sub>2</sub>O<sub>3</sub>-MgO-FeO retrieved welding fluxes formed in (a) Ar and (b) CO<sub>2</sub> welding atmosphere conditions.

alumino-silicates are replaced with comparatively simpler  $\text{TiO}_1$  structural units, the thermal conductivity of  $\text{TiO}_2$ -based fluxes is dominated by  $\text{TiO}_1$  structural units, and the greater presence of these structural units should increase the conductive heat transfer. These  $\text{TiO}_1$  structural units can typically form edge- and corner-sharing oligomers with other tetrahedral and polyhedral unit structures.

#### F. Welding Flux Electronegativity

Another important property of welding fluxes, which is often over-looked, is the electronegativity. This property can be correlated to arc condensation during

welding. Figure 17 shows the calculated average electronegativity according to  $\Lambda^{\text{corr}}$ , which corresponds to the tendency of an atom to attract electrons. Asokamnai and Manjula<sup>[47]</sup> defined an average electronegativity of superconducting oxides at high temperatures using the following Eq. [5].

$$\chi_{\text{lav}} = \frac{\sum_{i=1}^N X_i \times n_i}{N}, \quad [5]$$

where  $X_i$  is Pauling's electronegativity,<sup>[48]</sup>  $n_i$  is the number of atoms of each component, and  $N$  is the total number of components.<sup>[49]</sup> The results show that the trend of the inverse 'V-shape' in electronegativity as a function of  $\Lambda^{\text{corr}}$  is opposite to the results of the mechanical behavior, where a maximum peak in the electronegativity is observed contrary to the minimum in the mechanical properties near  $\Lambda^{\text{corr}}$  of 0.62.

According to Tseng and Chen,<sup>[8]</sup>  $\text{SiO}_2$  has a higher electronegativity than  $\text{TiO}_2$ ; thus, the root of the anode arc exhibits greater condensation with  $\text{SiO}_2$ -based fluxes than with  $\text{TiO}_2$ -based fluxes due to the change in arc condensation caused by the difference of electronegativity of each flux under similar experimental conditions. In addition, a flux having higher electronegativity extends the depth of the molten weld pool compared to its width, where the arc tends to be concentrated in the center direction of the weld pool by greater absorption of electrons. Other study has also suggested that higher electronegativity enhances the insulation effect of the flux, where arc voltage increases to maintain the current reduced by the flux resulting in deeper penetration.<sup>[50]</sup>

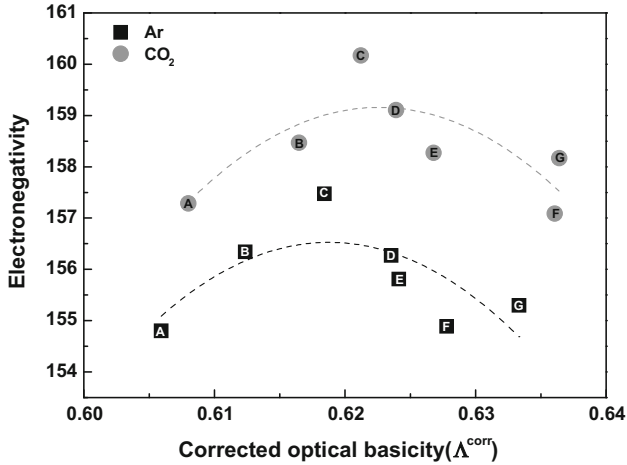


Fig. 17—Calculated electronegativity (dimensionless) of presented welding flux with corrected optical basicity.

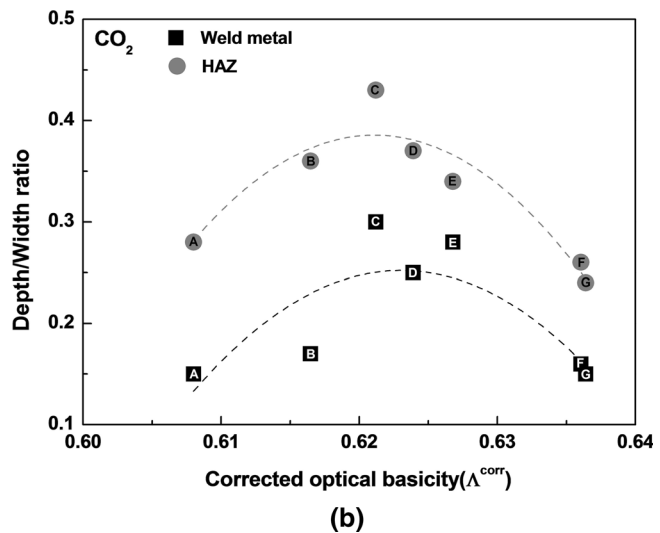
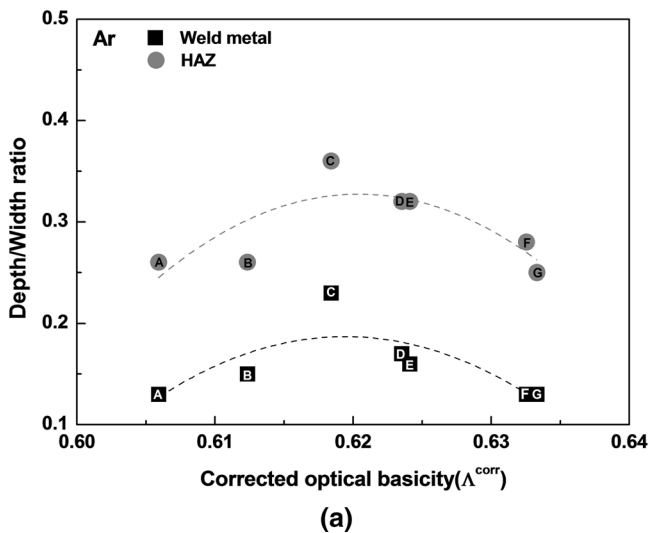


Fig. 18—Effect of corrected optical basicity on the depth-to-width ratios in weld metal and HAZ formed in (a) Ar and (b)  $\text{CO}_2$  welding atmosphere conditions.

The penetration depth-to-width ratio and the measured length are presented in Figures 18(a) and (b). The specimen welded with flux C shows the deepest penetration in both the weld metal and HAZ since flux C has the higher electronegativity due to the higher concentration of SiO<sub>2</sub>.

Dhandha and Badheka also suggested the effect of oxygen potential in the fusion zone and the change of surface tension of molten metals using the electronegativity of the components that comprise the fluxes, which results in the change of the Marangoni flow from the horizontal to the vertical direction of weld zone.<sup>[51]</sup>

Thus, the XPS oxygen anion analyses and structural analyses of the Raman measurement are well matched with the electronegativity trend, where the summation of the surface active components of O<sup>2-</sup> and O<sup>-</sup> and the TiO<sub>t</sub> structural units follows an inverse 'V-shape.' Thus, the conductive heat transfer can be affected by not only the flux structural units but also the electronegativity.

#### IV. CONCLUSIONS

Flux-cored arc welding wires with seven different TiO<sub>2</sub>-based flux compositions were designed for high Mn-containing AHSS. Welded specimens were machined and mechanically tested to fundamentally identify the relationship between the flux composition and mechanical properties such as tensile strength and micro-Vickers hardness. Post-welded fluxes were retrieved and analyzed using XRF, which was used to determine the thermo-physical properties of the fluxes.

1. The mechanical properties decreased until approximately 0.62 of the corrected optical basicity and increased oppositely. A valley shape of linearity was revealed with corrected optical basicity. The SEM and XRD analyses indicated that irregular ferrite phases were formed by fast cooling during the welding where fracture was occurred in, and a larger grain size of HAZ with a corrected optical basicity of approximately 0.62 was identified, while the other specimens, A and G, showed needle-shaped ferrite phases in the HAZ. Thus, the heat transfer of a flux can be considered the most important variable to understand the mechanical behavior.
2. According to UV-VIS-NIR spectrophotometry, it was obvious that phonon vibration affected the heat transport phenomenon only during welding, and radiation and reflection can be neglected. In addition, heat transfer by phonon vibration can be enhanced by the degree of polymerization of flux at high temperatures, which was revealed by optical analyses.
3. Thermo-physical properties such as wettability and viscosity were calculated and measured to identify the covering area on the bead and the degree of polymerization at high temperatures using the flux containing 6 wt pct Na<sub>2</sub>O as a fusing agent. All welding fluxes spread on a Pt-10Rh plate with full wetting instantly when the temperature reached 1773 K. This meant that the covering effect was

equal for all fluxes. The viscous behavior and degree of polymerization at high temperature increased in the order of G, A, and D, which well correlated with the heat transfer phenomenon.

4. Optical analyses, such as Raman, FTIR, and XPS, were conducted to identify the network structure of high TiO<sub>2</sub> containing welding flux system. As a result of the optical analyses, it was revealed that most of the complex network structures created by [AlO<sub>4</sub>]<sup>5-</sup> and [SiO<sub>4</sub>]<sup>4-</sup>-tetrahedral structures were already depolymerized by the basic oxides, and relatively simple structures based on TiO<sub>t</sub> units substituted them and altered the network structure, which resulted in the variation of heat transfer phenomenon. However, this can only be applied in the restricted condition where the network structure is highly depolymerized and TiO<sub>2</sub> content is dominant.
5. Electronegativity, a trend of attractive force to electrons, showed opposite behavior with the mechanical properties. A flux having high electronegativity can enhance arc stability and condense the arc area by the changes in the Marangoni flows. Thus, a deeper penetration can be realized. Subsequently, not only the thermal conductivity of the present welding flux but also the electronegativity affected the heat transfer phenomenon and direction during the welding process. In conclusion, both factors should be considered in the design of high TiO<sub>2</sub>-MnO-based multi-component welding flux system.

#### ACKNOWLEDGMENT

This study was supported by the Brain Korea 21 (BK21) Project of the Division of Humantronics Information Materials Grant No. 2017-11-0016 and the Ministry of Trade, Industry and Energy Grant No. 10044705.

#### REFERENCES

1. J.E. Jin and Y.K. Lee: *Mater. Sci. Eng. A*, 2009, vol. 527, pp. 157–61.
2. M.H. Cai, H. Ding, Z.Y. Tang, H.Y. Lee, and Y.K. Lee: *Steel Res. Int.*, 2011, vol. 82, pp. 242–48.
3. S. Kou: *Welding Metallurgy*, Wiley, Hoboken.
4. J.H.F. Gomes, S.C. Costa, A.P. Paiva, and P.P. Balestrassi: *J. Mater. Eng. Perform.*, 2012, vol. 21, pp. 1862–72.
5. J.E. Spear: *Occup. Health Saf.*, 2011, vol. 80, pp. 64–65.
6. J.S. Kim, Y.K. Woo, and B.Y. Lee: *J. KWJS*, 2012, vol. 30, pp. 304–08.
7. D.T. Cacic, G. Amza, C. Rontescu, S. Raise, and Z. Apostolescu: *Glob. J. Adv. Pure Appl. Sci.*, 2013, vol. 1, pp. 506–12.
8. K.H. Tseng, and K.L. Chen: *J. Nanosci. Nanotech.*, vol. 12, pp. 6359–67.
9. G. Qin, G. Wang, and Z. Zou: *Trans. Nonferrous Met. Soc. China*, 2012, vol. 22, pp. 23–29.
10. D.D. Schwemmer, D.L. Olson, and D.L. Williamson: *Weld. J.*, 1979, vol. 58, p. 153.
11. S. Datta, A. Bandyopadhyay, and P.K. Pal: *Int. J. Adv. Manuf. Technol.*, 2008, vol. 39, pp. 1136–43.

12. Standard, *Standard Test Methods for Tension Testing of Metallic Materials*, ASTM International, West Coshohocken, 2013.
13. C.S. Smith and L. Guttman: *Trans. AIME*, 1953, vol. 197, pp. 81–87.
14. K.C. Mills and S. Sridhar: *Ironmak. Steelmak.*, 1999, vol. 26, pp. 262–68.
15. S.H. Chung and I. Sohn: *Int. J. Hydr. Energy.*, 2015, vol. 40, pp. 15893–15900.
16. K.H. Tseng and P.Y. Chen: *Mater. Manuf. Process.*, 2016, vol. 31, pp. 359–65.
17. J.B. Kim and I. Sohn: *J. NonCryst. Solids*, 2013, vol. 379, pp. 235–43.
18. J.B. Kim, J.K. Choi, I.W. Han, and I. Sohn: *J. NonCryst. Solids*, 2016, vol. 432, pp. 218–26.
19. R.E. Boni and G. Derge: *JOM*, 1956, vol. 8, pp. 53–59.
20. J.B. Kim and I. Sohn: *ISIJ Int.*, 2014, vol. 54, pp. 2050–58.
21. F. Khodabakhshi, M. Haghshenas, H. Eskandari, and B. Koohbor: *Mater. Sci. Eng. A*, 2015, vol. 636, pp. 331–39.
22. R. Schroeder, G. Hammes, C. Binder, and A.N. Klein: *Mater. Res.*, 2011, vol. 14, pp. 564–68.
23. A.K. De, D.C. Murdock, M.C. Mataya, J.G. Speer, and D.K. Matlock: *Scr. Mater.*, 2004, vol. 50, pp. 1445–49.
24. X.L. Wan, R. Wei, and K.M. Wu: *Mater. Char.*, 2010, vol. 61, pp. 726–31.
25. S.S. Babu: *Curr. Opin. Solid State Mater. Sci.*, 2004, vol. 8, pp. 267–78.
26. R.O. Scattergood and C.C. Koch: *Scr. Metall. Mater.*, 1992, vol. 27, pp. 1195–1200.
27. P. Luo, D.T. McDonald, W. Xu, S. Palanisamy, M.S. Dargusch, and K. Xia: *Scr. Mater.*, 2012, vol. 66, pp. 785–88.
28. J.Y. Park and I. Sohn: *Int. J. Heat Mass Tran.*, 2017, vol. 109, pp. 1014–25.
29. S.W. Park and I. Sohn: *J. Am. Ceram. Soc.*, 2016, vol. 99, pp. 612–18.
30. A. Nagashima: *Int. J. Thermophys.*, 1990, vol. 11, pp. 417–32.
31. K.C. Mills: *ISIJ Int.*, 1993, vol. 33, pp. 148–55.
32. D.W. Lee and W.D. Kingery: *J. Am. Ceram. Soc.*, 1960, vol. 43, pp. 594–607.
33. M. Susa, A. Kushimoto, H. Toyota, M. Hayashi, R. Endo, and Y. Kobayashi: *ISIJ Int.*, 2009, vol. 49, pp. 1722–29.
34. M. Susa, A. Kushimoto, R. Endo, and Y. Kobayashi: *ISIJ Int.*, 2011, vol. 51, pp. 1587–96.
35. M. Susa, S. Kubota, M. Hayashi, and K.C. Mills: *Ironmak. Steelmak.*, 2001, vol. 28, pp. 390–95.
36. S. Ozawa, M. Susa, T. Goto, R. Endo, and K.C. Mills: *ISIJ Int.*, 2006, vol. 46, pp. 413–19.
37. M. Susa, F. Li, and K. Nagata: *Metall. Trans. B*, 1992, vol. 23, pp. 331–37.
38. E.J. Jung and D.J. Min: *Steel Res. Int.*, 2012, vol. 83, pp. 705–11.
39. D. Bonn, J. Eggers, J. Indekeu, J. Meunier, and E. Rolley: *Rev. Mod. Phys.*, 2009, vol. 81, pp. 739–805.
40. I. Sohn and D.J. Min: *Steel Res. Int.*, 2012, vol. 83, pp. 611–30.
41. B. Reynard and S.L. Webb: *Eur. J. Mineral.*, 1998, vol. 10, pp. 49–58.
42. J.Y. Park, J.G. Park, C.H. Lee, and I. Sohn: *ISIJ Int.*, 2011, vol. 51, pp. 889–94.
43. C. Le Losq, D.R. Neuville, P. Florian, G.S. Henderson, and D. Massiot: *Geochim. Cosmochim. Acta*, 2014, vol. 126, pp. 495–517.
44. N.J. Hess, Y. Su, and M.L. Balmer: *J. Phys. Chem. B*, 2001, vol. 105, pp. 6805–11.
45. P. McMillan and B. Piriou: *J. NonCryst. Solids*, 1983, vol. 55, pp. 221–42.
46. G.W. Toop and C.S. Samis: *Trans. AIME*, 1962, vol. 224, pp. 878–87.
47. R. Asokamani and R. Manjula: *Phys. Rev. B*, 1989, vol. 39, pp. 4217–21.
48. L. Pauling: *The Nature of the Chemical Bond and the Structure of Molecules and Crystals: an Introduction to Modern Structural Chemistry*, Cornell University Press, Ithaca, 1960.
49. R.R. Reddy, Y. Nazeer Ahammed, P. Abdul Azeem, K. Rama Gopal, and T.V.R. Rao: *J. NonCryst. Solids*, 2001, vol. 286, pp. 169–80.
50. P.J. Modenesi, E.R. Apolinário, and I.M. Pereira: *J. Mater. Process. Technol.*, 2000, vol. 99, pp. 260–65.
51. K.H. Dhandha and V.J. Badheka: *J. Manuf. Process.*, 2015, vol. 17, pp. 48–57.